

COG: Confidence-aware Optimal Geometric Correspondence for Unsupervised Single-reference Novel Object Pose Estimation

Yuchen Che¹ Jingtu Wu¹ Hao Zheng² Asako Kanezaki^{1,2,3}

¹Institute of Science Tokyo ²RIKEN ³Tohoku University

{che.y.99ea@m, wu.j.baa4@m, kanezaki@comp}.isct.ac.jp, hao.zheng@riken.jp

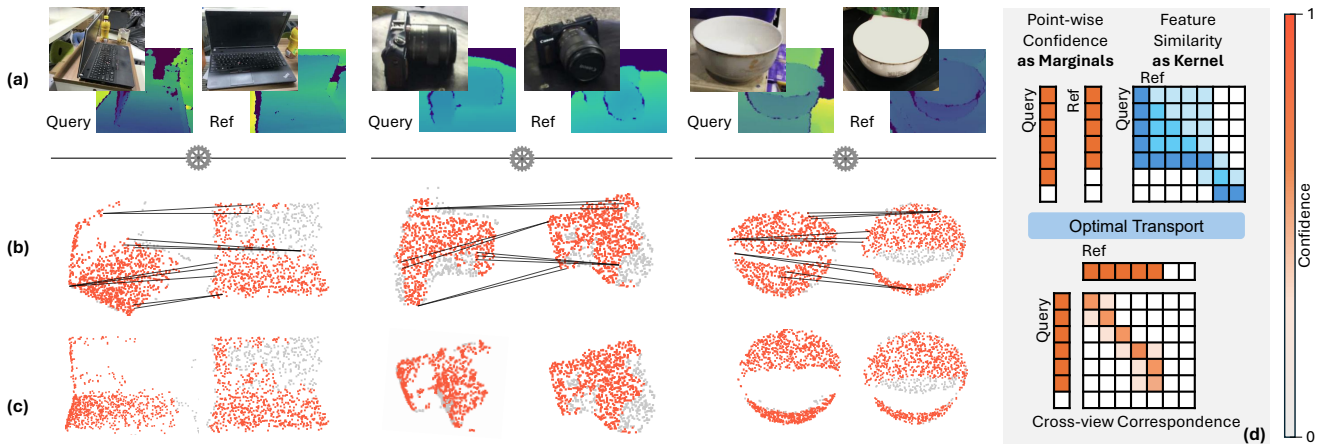


Figure 1. Given a novel object’s query and reference RGB-D images (a), COG outputs point-wise confidence and cross-view soft correspondence (b), to estimate the relative pose between query and reference (c). To achieve this, we formulate correspondence finding as an optimal transport problem, with each point’s confidence as target marginals, and the point features’ similarity as an affinity kernel (d).

Abstract

Estimating the 6DoF pose of a novel object with a single reference view is challenging due to occlusions, view-point changes, and outliers. A core difficulty lies in finding robust cross-view correspondences, as existing methods often rely on discrete one-to-one matching that is non-differentiable and tends to collapse onto sparse keypoints. We propose Confidence-aware Optimal Geometric Correspondence (COG), an unsupervised framework that formulates correspondence estimation as a confidence-aware optimal transport problem. COG produces balanced soft correspondences by predicting point-wise confidences and injecting them as optimal transport marginals, suppressing non-overlapping regions. Semantic priors from vision foundation models further regularize the correspondences, leading to stable pose estimation. This design integrates confidence into the correspondence finding and pose estimation pipeline, enabling unsupervised learning. Experiments show unsupervised COG achieves comparable performance to supervised methods, and supervised COG outperforms them. Codes: <https://github.com/YC-Che/COG>

1. Introduction

Object pose estimation, which aims to recover an object’s 6DoF pose (rotation and translation) from RGB-D images, is a fundamental task for robotics [20, 21, 62], augmented reality [42, 57], and 3D scene understanding [30, 74]. To enable general real-world deployment, improving the generalization capability of object pose estimation has long been a central goal. Early instance-level methods [28, 64, 66, 71] assume access to CAD models or training objects identical to those at test time. This assumption was relaxed in category-level pose estimation [7, 32, 67, 68], where models learn to estimate the poses of unseen instances within a few predefined categories.

Recent research has advanced toward novel object pose estimation [9, 27, 35, 39, 44, 58], which targets poses of arbitrary objects with dataset-agnostic generalization. However, these methods often depend on CAD models or multiple reference views, which limits scalability in practice. A more challenging setting considers only a single reference image [18, 40, 41, 46] (see Fig. 1), where large view-point changes and partial observations require the network to jointly infer valid overlapping regions and object pose,

making the problem particularly ill-posed. A key to solving this task is to establish reliable cross-view correspondences, since the pose can be recovered by aligning geometric structures between query and reference views. Yet, most existing approaches [39, 41] construct correspondences via discrete one-to-one assignments (*e.g.* argmax), which tend to collapse onto a few dominant keypoints, leaving many of the points unused. Moreover, such non-differentiable assignments breaks differentiability and prevents the model from being trained in an unsupervised manner.

We introduce Confidence-aware Optimal Geometric Correspondence (COG), an unsupervised framework for novel object pose estimation from a single reference image. COG addresses the above issues by formulating soft correspondence as an optimal transport (OT) problem, where point-wise confidences are predicted beforehand and explicitly incorporated as target marginals of the transport plan. Compared to OT-based methods [13, 55, 72] with uniform marginals and only apply confidence post hoc, This formulation yields globally balanced correspondences that naturally suppresses outliers and non-overlapping regions. Given these correspondences, corresponding points are generated via convex combinations, and a weighted SVD solver [63] is used to recover the pose transformation. The entire process forms an end-to-end correspondence finding and pose estimation pipeline, enabling unsupervised optimization of both correspondence and confidence. To mitigate ambiguity in purely geometric matching, we integrate semantic priors denoised from vision foundation models such as DINO [5, 48], which softly encourage correspondences between semantically consistent parts. Furthermore, for unsupervised confidence learning, Gaussian RBF-style kernels of geometric and semantic consistency are used to generate pseudo confidence labels, guiding the network to down weight uncertain points without discarding them entirely and to emphasize reliable regions with high confidence. With these designs, COG naturally extends to the unsupervised setting, where neither ground-truth confidence nor pose supervision is available. Experimental results demonstrate that COG achieves performance comparable to leading supervised approaches, while the supervised variant of COG further outperforms them.

Our contributions are summarized as follows:

1. We formulate correspondence finding as an OT problem with confidence as marginals. Compared to OT with uniform marginals, our formulation yields balanced correspondences by suppressing non-overlapping points.
2. We propose an end-to-end pipeline that jointly learns object pose and point validity confidence without supervision from CAD models, poses, or overlap scores.
3. Unsupervised COG achieves performance competitive with state-of-the-art supervised methods, and its supervised variant further outperforms them.

2. Related Work

Instance-level and Category-level Object Pose Estimation. Traditional object pose estimation methods, under both instance-level [26, 28, 64, 66, 71] and category-level [7, 22, 32, 38, 67, 68] settings, aim to recover the 6DoF poses of known objects or objects within predefined categories. A common paradigm is to directly regress object poses [10, 14, 77] using deep backbones. Alternatively, correspondence-based approaches establish matches either between CAD models and point clouds [31, 32, 61], or between query images and rendered CAD views [59, 65, 68], followed by transformation estimation via PnP [36] or Umeyama [63]. Recently, unsupervised or weakly supervised frameworks have also gained attention. EquiPose [38] jointly learns canonical reconstruction and pose using $SE(3)$ -equivariant backbones [8, 79], while OP-Align [7] extends this paradigm to articulated objects. Zero-shot Pose [24] aligns semantic features across image sequences to establish correspondences without explicit pose labels. However, these settings inherently limit generalization, as they rely on prior knowledge of specific object instances or categories, restricting their ability to handle novel objects in open-world scenarios.

Novel Object Pose Estimation. Novel object pose estimation lifts the instance-level and category-level restriction by targeting arbitrary objects beyond predefined categories. For such dataset-agnostic generalization, many approaches [4, 9, 39, 41] exploit vision foundation models [5, 48, 52] to extract semantic priors for correspondence learning. Further progress [9, 27, 35, 39, 44, 47, 58] leverages additional references such as CAD models or multi-view images to construct dense correspondences. For example, SAM-6D [39] builds on CNOS [45] by using SAM [34, 76] for segmentation and combining DINO [48] features with geometric cues, while OnePose [27, 58] reconstructs object point clouds via Structure-from-Motion and aligns them to query views. MegaPose [35] retrieves the closest CAD rendering to the query for subsequent refinement, and GenFlow [44] iteratively refines poses by estimating optical flow between rendered and observed views. More recently, several methods attempt to reduce reference requirements to a single image [18, 40, 41, 46]. POPE [18] and NOPE [46] introduce feedforward frameworks with RGB inputs, While SinRef-6D [40] models point-wise alignment using state-space dynamics with RGB-D inputs, and the latest UnoPose [41] constructs an $SE(3)$ -invariant canonical frame for consistent object representation. Yet, most existing approaches construct correspondences via discrete one-to-one assignments, which tend to collapse onto a few dominant keypoints, and breaks differentiability, preventing models from being trained in an unsupervised manner.

Point Cloud Registration. As a commonly used formulation in object pose estimation, correspondence finding and pose estimation can also be viewed from the perspective of point cloud registration [11, 12, 16, 23, 37, 49, 54, 72], which seeks to estimate the optimal rigid transformation that aligns two partially overlapping point sets. A common pipeline extracts discriminative local descriptors to establish correspondences, followed by robust solvers such as RANSAC [19] and ICP [1, 2]. FCGF [11] and DGR [12] enhance this process by predicting pairwise inlier probabilities to filter unreliable matches. More recent methods [13, 43, 55, 72, 73] formulate registration as an optimal transport (OT) problem, treating correspondences as continuous probability distributions. RPM-Net [72] introduces a differentiable Sinkhorn [56] layer to compute correspondences under uniform marginals. Meanwhile, confidence which represents the validity of correspondences has also been explored—either as post-hoc calibration of pairwise matches [73], as distribution-level weights [43], or as the results of a global thresholding [13]. These OT-based methods typically assign such weights after the correspondences have been established, making the correspondences still unbalanced. And more importantly, the resulting confidence cannot be optimized jointly with the correspondences in an end-to-end manner. In contrast, we propose a learned point-wise confidence that directly serves as the target marginal in OT, yielding globally balanced transport plans and enable end-to-end unsupervised learning.

3. Methodology

3.1. Problem Formulation

Given two RGB-D images of the same novel object captured from different viewpoints, one as the query and the other as the reference, our goal is to estimate the relative rigid transformation between them. As illustrated in Fig. 2, we first employ a CNOS [45]-like segmentation model, UnoSeg [41], to obtain object masks from the RGB images. The masked depth maps are then back-projected into 3D space to generate point clouds. In addition to geometric coordinates, we extract per-pixel RGB features using DINO [48] (patch features with up-sampling), which serve as RGB descriptors. We denote the query and reference point clouds as $\mathbf{P} \in \mathbb{R}^{n \times 3}$ and $\mathbf{Q} \in \mathbb{R}^{n \times 3}$, and their associated RGB features as $\mathbf{F}_p \in \mathbb{R}^{n \times d_f}$ and $\mathbf{F}_q \in \mathbb{R}^{n \times d_f}$, where n is the number of points and d_f is the dimension of the DINO features. Our objective is to find a rotation $\mathbf{R}_{pq} \in SO(3)$ and a translation $\mathbf{t}_{pq} \in \mathbb{R}^3$ such that

$$\mathbf{Q}^{\text{val}} = \mathbf{P}^{\text{val}} \mathbf{R}_{pq} + \mathbf{1} \mathbf{t}_{pq}^{\top}, \quad (1)$$

where $\mathbf{P}^{\text{val}} \subset \mathbf{P}$ and $\mathbf{Q}^{\text{val}} \subset \mathbf{Q}$ denote the valid overlapping regions of the object that can be matched across views. Since the observed point clouds \mathbf{P} and \mathbf{Q} are often partial

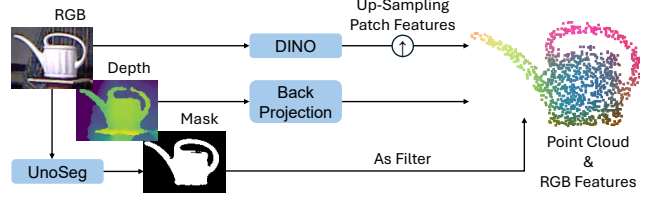


Figure 2. Pre-processing pipeline of COG. Given RGB-D inputs, an object is segmented, depth map is back-projected into point clouds, and per-point RGB features are extracted from DINO to form feature augmented inputs.

due to occlusions and viewpoint differences, this task inherently requires reasoning about both the relative pose and the validity of each point. For clarity, throughout this paper the subscripts pq and qp denote operations in the query-to-reference and reference-to-query directions, respectively.

3.2. COG

3.2.1. Model Overview

As illustrated in Fig. 3, COG adopts a coarse-to-fine architecture built upon a geometric transformer [51]. In the coarse phase, we use farthest point sampling [17] to obtain sparse point clouds and their DINO features as inputs (denoted with $\tilde{\cdot}$), while in the fine phase, the full point clouds and DINO features are used for refinement. For clarity, we use the fine phase notation throughout the following sections; the coarse phase shares the same formulation with all terms marked by $\tilde{\cdot}$.

Specifically, the geometric transformer encoder takes the query and reference point sets \mathbf{P} and \mathbf{Q} as inputs to the $SE(3)$ -invariant feature encoding module (and to the position embedding module in the fine phase), producing geometric hidden features \mathbf{H}_p and \mathbf{H}_q . Meanwhile, DINO features are processed through a semantic denoising module to obtain semantic embeddings $\mathbf{S}_p \in \mathbb{R}^{n \times d_s}$ and $\mathbf{S}_q \in \mathbb{R}^{n \times d_s}$. The geometric decoder then applies alternating self-attention and cross-attention layers to compute point-wise geometric features $\mathbf{G}_p \in \mathbb{R}^{n \times d_g}$ and $\mathbf{G}_q \in \mathbb{R}^{n \times d_g}$. Then a lightweight MLP confidence head with a sigmoid activation outputs per-point confidence scores $\mathbf{c}_p, \mathbf{c}_q \in [0, 1]^n$. These confidence values are normalized into $\mathbf{w}_p = \mathbf{c}_p / \overline{\mathbf{c}_p}$, $\mathbf{w}_q = \mathbf{c}_q / \overline{\mathbf{c}_q}$, and incorporated as target marginals in an optimal transport formulation, while the cosine similarity between geometric and semantic features forms the affinity kernel $\mathbf{K} \in \mathbb{R}^{n \times n}$. We apply the Sinkhorn algorithm [56] to solve for the transport plan $\Pi \in [0, 1]^{n \times n}$ and derive the row-stochastic correspondence matrices $\mathbf{M}_{pq}, \mathbf{M}_{qp} \in [0, 1]^{n \times n}$. Using these correspondences as projection operators, we compute soft matches $\mathbf{M}_{pq} \mathbf{Q}$ and $\mathbf{M}_{qp} \mathbf{P}$ via convex combination, and estimate the rigid transformation using weighted SVD [63], where normalized confidence weights \mathbf{w}_p and \mathbf{w}_q emphasize reliable correspondences. After the coarse

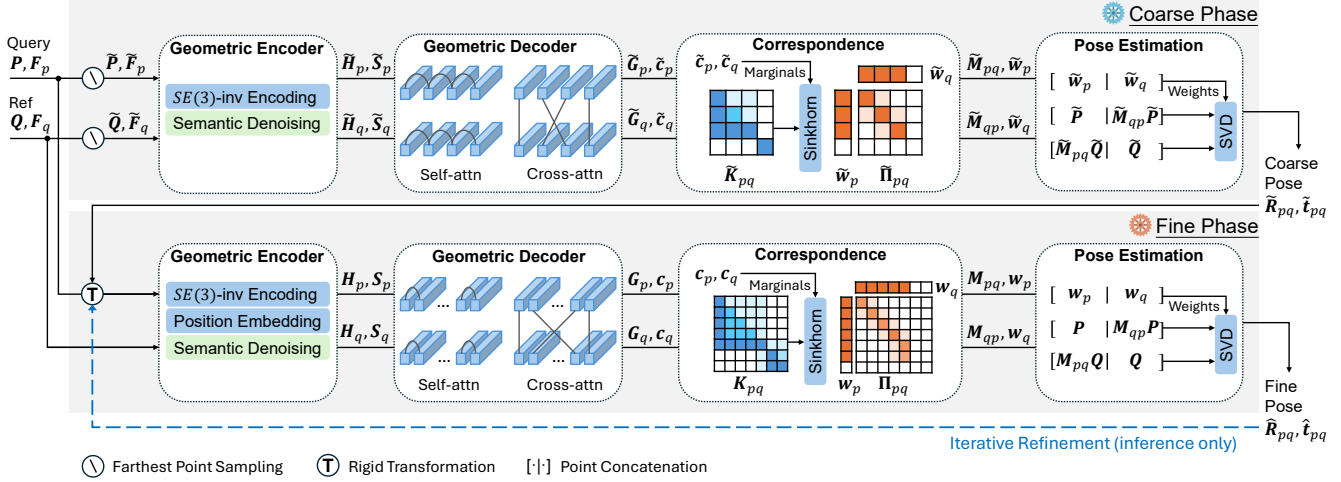


Figure 3. Overview of the COG framework. The pipeline consists of coarse and fine phases, each using a geometric transformer to predict point-wise confidences and features. A Sinkhorn-based OT module computes soft correspondences, and a weighted SVD solver estimates the rigid transformation. The coarse pose is further refined in the fine phase using position embeddings for precise alignment.

phase, the estimated pose ($\tilde{\mathbf{R}}_{pq}, \tilde{\mathbf{t}}_{pq}$) is applied to transform the query cloud, producing a coarse aligned version used in the fine phase to predict the final refined pose ($\hat{\mathbf{R}}_{pq} \in SO(3)$, $\hat{\mathbf{t}}_{pq} \in \mathbb{R}^3$). During inference, iterative refinement is applied by repeatedly transforming the query cloud using the estimated pose, further improving alignment accuracy.

We next introduce the optimal transport based correspondence formulation in Sec. 3.2.2, followed by pose estimation in Sec. 3.2.3, semantic priors in Sec. 3.2.4, and confidence learning in Sec. 3.2.5.

3.2.2. Optimal Correspondence

In our formulation, the confidence of each point represents its likelihood of finding a valid correspondence in the counterpart point cloud. Thus, correspondence estimation between the query and reference can be interpreted as transporting these confidence weights from one distribution to the other. This perspective naturally casts the problem as an optimal transport (OT) task, where the transport plan satisfies marginal constraints approximately consistent with the predicted confidences. Such a formulation ensures globally balanced soft correspondences and prevents over concentration on a few dominant keypoints.

We first construct an affinity kernel that combines geometric and semantic similarities as

$$\mathbf{K}_{[i,j]} = \exp\left(\frac{1}{\tau} \langle \mathbf{G}_{p[i]}, \mathbf{G}_{q[j]} \rangle_{\cos}\right) (1 + \langle \mathbf{S}_{p[i]}, \mathbf{S}_{q[j]} \rangle_{\cos})^{\lambda/\tau}, \quad (2)$$

where τ and λ are temperature and semantic prior weight hyper-parameters. To handle cases where the two point clouds exhibit different confidence distributions, we normalize the predicted confidences by their means to form target marginals $\mathbf{w}_p = \mathbf{c}_p / \bar{\mathbf{c}}_p$ and $\mathbf{w}_q = \mathbf{c}_q / \bar{\mathbf{c}}_q$, ensuring that $\sum_i \mathbf{w}_{p[i]} = \sum_j \mathbf{w}_{q[j]} = n$. This normalization

preserves global balance and allows sparse high-confidence regions to distribute their mass over denser ones. The transport plan $\mathbf{\Pi} = \mathcal{S}(\mathbf{K}, \mathbf{w}_p, \mathbf{w}_q) \in [0, 1]^{n \times n}$ is obtained using the Sinkhorn algorithm [56] (denotes with \mathcal{S}), where $\sum_j \mathbf{\Pi}_{[i,j]} \approx \mathbf{w}_{p[i]}$ and $\sum_i \mathbf{\Pi}_{[i,j]} \approx \mathbf{w}_{q[j]}$. We then normalize $\mathbf{\Pi}$ row-wise to derive directional, row-stochastic correspondence matrices, such as $\mathbf{M}_{pq}[i,j] = \frac{\mathbf{\Pi}_{[i,j]}}{\sum_k \mathbf{\Pi}_{[i,k]}}$, and $\mathbf{M}_{qp}[i,j] = \frac{\mathbf{\Pi}_{[i,j]}^T}{\sum_k \mathbf{\Pi}_{[i,k]}}$. Here, \mathbf{M}_{pq} and \mathbf{M}_{qp} act as soft projection operators, mapping each point in one cloud to a convex combination of points in the other. Accordingly, we denote $\mathbf{M}_{pq}\mathbf{Q}$ as the corresponding points of \mathbf{P} in the \mathbf{Q} space, and $\mathbf{M}_{qp}\mathbf{P}$ vice versa.

To regularize the correspondences, we enforce a cycle consistency constraint inspired by CycleGAN [78]. A point be projected to the opposite domain and back with \mathbf{M}_{pq} and \mathbf{M}_{qp} should approximately reconstruct its original position. The cycle consistency loss is defined as

$$\mathcal{L}_{\text{cycl}} = \frac{1}{n} \sum_{i=1}^n \mathbf{w}_{p[i]} \left(1 - \phi_{\text{cycl}}(\mathbf{P}, \mathbf{P}^{\text{rec}})_{[i]}\right) + \frac{1}{n} \sum_{j=1}^n \mathbf{w}_{q[j]} \left(1 - \phi_{\text{cycl}}(\mathbf{Q}, \mathbf{Q}^{\text{rec}})_{[j]}\right), \quad (3)$$

where $\mathbf{P}^{\text{rec}} = \mathbf{M}_{pq}\mathbf{M}_{qp}\mathbf{P}$ and $\mathbf{Q}^{\text{rec}} = \mathbf{M}_{qp}\mathbf{M}_{pq}\mathbf{Q}$. The kernel ϕ_{cycl} measures geometric similarity via a Gaussian RBF:

$$\phi_{\text{cycl}}(\mathbf{X}, \mathbf{Y})_{[i]} = \exp\left(-\alpha_g \|\mathbf{X}_{[i]} - \mathbf{Y}_{[i]}\|_2^2\right), \quad (4)$$

where α_g is a geometric scaling parameter and $\mathbf{X}, \mathbf{Y} \in \mathbb{R}^{n \times 3}$ are point clouds.

3.2.3. Pose Estimation

Once the correspondence matrices and point-wise confidences are obtained, we estimate the 6DoF rigid transformation between the query and reference using a confidence-weighted SVD, Umeyama algorithm [63], also known as corresponding point alignment [53]. This algorithm takes two point sets with associated correspondences and per-point weights as input, and outputs the optimal rotation and translation minimizing the weighted least squares error.

For the consistency, we concatenate both sides correspondences with the original point clouds, and perform joint optimization as

$$\hat{\mathbf{R}}_{pq}, \hat{\mathbf{t}}_{pq} = \mathcal{U}([\mathbf{P} | \mathbf{M}_{qp}\mathbf{P}], [\mathbf{M}_{pq}\mathbf{Q} | \mathbf{Q}], [\mathbf{w}_p | \mathbf{w}_q]), \quad (5)$$

where $\mathcal{U}(\cdot)$ denotes the Umeyama solver, and $[\mathbf{X} | \mathbf{Y}] \in \mathbb{R}^{2n \times 3}$ represents concatenation along the point dimension. The inverse transformation is naturally given by $\hat{\mathbf{R}}_{qp} = \hat{\mathbf{R}}_{pq}^\top$ and $\hat{\mathbf{t}}_{qp} = -\hat{\mathbf{R}}_{pq}^\top \hat{\mathbf{t}}_{pq}$. The transformed point clouds are thus $\mathbf{P}^{\text{pred}} = \mathbf{P}\hat{\mathbf{R}}_{pq} + \mathbf{1}\hat{\mathbf{t}}_{pq}^\top$ and $\mathbf{Q}^{\text{pred}} = \mathbf{Q}\hat{\mathbf{R}}_{qp} + \mathbf{1}\hat{\mathbf{t}}_{qp}^\top$.

The estimated poses are optimized using a confidence-weighted Chamfer loss that measures geometric alignment between the transformed and target point clouds, defined as

$$\begin{aligned} \mathcal{L}_{\text{pose}} = & \frac{1}{n} \sum_{i=1}^n \mathbf{w}_p[i] \left(1 - \phi_{\text{pose}}(\mathbf{P}, \mathbf{Q}^{\text{pred}})_{[i]} \right) \\ & + \frac{1}{n} \sum_{j=1}^n \mathbf{w}_q[j] \left(1 - \phi_{\text{pose}}(\mathbf{Q}, \mathbf{P}^{\text{pred}})_{[j]} \right), \end{aligned} \quad (6)$$

where ϕ_{pose} is a Gaussian RBF kernel based on the Chamfer distance [69]:

$$\phi_{\text{pose}}(\mathbf{X}, \mathbf{Y})_{[i]} = \exp\left(-\alpha_g \min_{j \in \{1, \dots, n\}} \|\mathbf{X}_{[i]} - \mathbf{Y}_{[j]}\|_2^2\right), \quad (7)$$

with α_g a geometric scaling hyperparameter and $\mathbf{X}, \mathbf{Y} \in \mathbb{R}^{n \times 3}$ denoting point clouds.

3.2.4. Semantic Priors

Semantic features provide valuable cues for establishing reliable correspondences, as they help constrain matches within semantically consistent regions. To leverage such cues, we incorporate semantic priors derived from vision foundation models (VFM) such as DINOv2 [48], which produce patch level RGB embeddings capturing high level visual semantics. However, we observe that raw DINO features, while semantically rich, often encode mixed information unrelated to object parts, resulting in feature inconsistencies across viewpoints. Points belonging to the same semantic part may still exhibit noticeable differences in feature space, degrading cross-view matching quality. To improve their robustness, we adopt the self label refinement strategy of STEGO [25], which applies energy based clustering for semantic denoising and yields more stable and

consistent features. In our model, a lightweight semantic head (an MLP) projects the DINO features \mathbf{F}_p and \mathbf{F}_q into lower dimensional semantic embeddings \mathbf{S}_p and \mathbf{S}_q . The semantic head is trained with the same loss as STEGO, promoting feature consistency across corresponding regions while filtering noise.

To softly constrain the correspondence using semantic similarity, we define a semantic consistency loss that penalizes correspondences assigned to semantically dissimilar points. Formally,

$$\begin{aligned} \mathcal{L}_{\text{sem}} = & \frac{1}{n} \sum_{i=1}^n \mathbf{w}_p[i] \left(1 - \phi_{\text{sem}}(\mathbf{M}_{pq}, \mathbf{S}_p, \mathbf{S}_q)_{[i]} \right) \\ & + \frac{1}{n} \sum_{j=1}^n \mathbf{w}_q[j] \left(1 - \phi_{\text{sem}}(\mathbf{M}_{qp}, \mathbf{S}_q, \mathbf{S}_p)_{[j]} \right), \end{aligned} \quad (8)$$

where ϕ_{sem} measures feature similarity through a Gaussian RBF kernel weighted by the correspondence matrix:

$$\begin{aligned} \phi_{\text{sem}}(\mathbf{M}_{uv}, \mathbf{U}, \mathbf{V})_{[i]} = & \\ & \sum_{j=1}^n \mathbf{M}_{uv}[i, j] \exp\left(-\alpha_f (1 - \langle \mathbf{U}_{[i]}, \mathbf{V}_{[j]} \rangle_{\cos})\right), \end{aligned} \quad (9)$$

where $\mathbf{M}_{uv} \in [0, 1]^{n \times n}$ is a row-stochastic correspondence matrix, $\mathbf{U}, \mathbf{V} \in \mathbb{R}^{n \times d}$ are semantic feature matrices, and α_f is a scaling hyperparameter. This loss encourages correspondences to align semantically coherent regions while maintaining the soft matching flexibility of OT.

3.2.5. Confidence Learning

The absence of ground-truth confidence labels poses a key challenge for unsupervised training. We address this by constructing pseudo confidence labels derived from the model’s own geometric and semantic consistency quality. Intuitively, a reliable (high confidence) point should incur low loss values, corresponding to high values of the Gaussian RBF kernels ϕ_{cycl} , ϕ_{pose} , and ϕ_{sem} . Hence, these kernel responses can be interpreted as soft inlier likelihoods that jointly reflect geometric, semantic, and cyclic consistency.

Formally, we define a composite pseudo likelihood as $\phi_{\text{tot}}(\cdot) = \phi_{\text{cycl}}(\cdot) \phi_{\text{pose}}(\cdot) \phi_{\text{sem}}(\cdot)$, to generate pseudo confidence labels: $\mathbf{z}_p = \phi_{\text{tot}}(\mathbf{P}, \mathbf{P}^{\text{rec}}, \mathbf{Q}^{\text{pred}}, \mathbf{M}_{pq}, \mathbf{S}_p, \mathbf{S}_q)$, and $\mathbf{z}_q = \phi_{\text{tot}}(\mathbf{Q}, \mathbf{Q}^{\text{rec}}, \mathbf{P}^{\text{pred}}, \mathbf{M}_{qp}, \mathbf{S}_q, \mathbf{S}_p)$. These labels provide graded supervision instead of binary inlier-outlier signals, enabling the confidence branch to learn to down weight uncertain points rather than discard them. By jointly fusing cues from geometric reconstruction, pose alignment, and semantic consistency, the pseudo labels capture complementary aspects of correspondence reliability and yield well calibrated confidence predictions. The confidence is

optimized using a binary cross entropy (BCE) loss:

$$\mathcal{L}_{\text{conf}} = \text{BCE}(\mathbf{c}_p, \text{detach}(\mathbf{z}_p)) + \text{BCE}(\mathbf{c}_q, \text{detach}(\mathbf{z}_q)), \quad (10)$$

where detach indicates a stop-gradient operation to prevent gradients from propagating into other loss terms, ensuring that $\mathcal{L}_{\text{conf}}$ serves purely as supervision for confidence.

4. Experiments

4.1. Experimental Settings

Datasets and Benchmarks. Following MegaPose [35], we train COG on two large-scale datasets: Google Scanned Objects [15] and ShapeNet [6]. Together, these datasets contain approximately 2,000,000 RGB-D images of over 50,000 objects covering diverse shapes and materials. For evaluation, we adopt BOP [60] benchmarks, TUD-L, LM-O, and YCB-V [3, 29, 70], which test generalization to unseen objects and complex scenes. Specifically, TUD-L includes 600 images of 3 geometrically intricate objects; LM-O contains 200 images of 8 objects in a cluttered tabletop scene; and YCB-V provides 900 images of 21 household objects, sometimes heavily occluded.

Implementation Details. We use the same backbone as our direct baseline UnoPose [41]: the coarse phase encoder-decoder is implemented as standard geometric transformer [51], while the fine phase adopts a sparse-to-dense variant introduced in [39]. We also re-implement Robust OT [55] and Dustbin OT [13] with these backbones. For fair comparison, we use the same query-reference pairing and the same segmentation masks as UnoPose for all models. We train using the ADAM optimizer [33] with an initial learning rate of 10^{-4} . The model is trained for 3 epochs with a batch size of 32. The loss weights are set to $\gamma_{\text{cycl}} = 0.5$, $\gamma_{\text{pose}} = 1$, $\gamma_{\text{sem}} = 1$, and $\gamma_{\text{conf}} = 10$. Hyperparameters are $\lambda = 3$, $\tau = 0.01$, $\alpha_f = 4$, and $\alpha_g = 60$. We randomly sample 1024 points from both query and reference point clouds as input to the fine phase, and 256 points via farthest point sampling [17] for the coarse phase. Additionally, we train a supervised variant of COG by only replacing the Chamfer distance in $\mathcal{L}_{\text{pose}}$ with the point-wise distance between the predicted and ground-truth transformed points $(\mathbf{P}\mathbf{R}_{pq} + \mathbf{1}\mathbf{t}_{pq}^{\top})_{[i]}$ and $(\mathbf{P}\hat{\mathbf{R}}_{pq} + \mathbf{1}\hat{\mathbf{t}}_{pq}^{\top})_{[i]}$.

Evaluation Metrics. For pose evaluation, we follow the BOP protocol, report mean Average Precision (mAP) under three standard error metrics: VSD, MSSD, and MSPD (see [60] for definitions). We also report the average inference time, including both segmentation and pose estimation modules. For overlapping evaluation, we report the Intersection-over-Union (IoU) between the predicted and the GT overlapping regions.

4.2. Results

4.2.1. Object Pose Estimation

Quantitative and qualitative results for single-reference novel object pose estimation are presented in Tab. 1 and Fig. 4, respectively. COG, when trained in an unsupervised manner, not only outperforms all other unsupervised baselines but also outperforms most supervised methods. Compared with the state-of-the-art supervised approach UnoPose [41], our unsupervised model achieves comparable performance, with only a 2.1% gap on average. Notably, on benchmark with relatively complicated object shapes, TUD-L, our unsupervised method exceeds UnoPose for 2.8%. Meanwhile, on benchmarks characterized by cluttered scenes and heavily occlusions, LM-O and YCB-V, performance gap increases, suggesting that unsupervised training still has room for improvement in handling complicated environments. When trained with pose supervision, COG achieves the best overall performance across LM-O and TUD-L, outperforming all existing methods. In particular, the large improvement on TUD-L highlights the model’s robustness in accurately capturing fine-grained geometric correspondences. Compared to other OT-based methods, Robust OT [55], Dustbin OT [13], and RPM-Net [72], our method exceeds them on all benchmarks, indicating the efficiency of confidence marginal OT and network-predicted confidence rather than post hoc calibration. Overall, these results demonstrate that COG achieves performance competitive with supervised methods even without ground-truth supervision, and that its supervised variant further establishes a new state of the art. This validates the effectiveness of our confidence-aware OT formulation and the unsupervised network-predicted confidence.

4.2.2. Overlapping Prediction

As an essential step toward accurate pose estimation, we also evaluate the overlapping prediction derived from the confidence values. Predicted confidence values greater than 0.5 are treated as positives, while others are negatives. Tab. 2 reports the IoU between predicted and ground-truth overlapping regions on the TUD-L dataset, and qualitative examples are shown in the last 3 columns of Fig. 5. COG effectively distinguishes overlapping from non-overlapping areas by assigning high confidence to valid points and low confidence to outliers and semantic or geometric inconsistent points. Even without supervision, our method exceeds the supervised UnoPose’s performance in average, and the visualization demonstrate that the learned confidence is both interpretable and robust for outliers.

4.3. Ablation Studies

4.3.1. Modules and Losses

To evaluate the contribution of different correspondence formulations and loss terms, we conduct ablation studies

Method	Supervision	Modality	Reference	LM-O [3] \uparrow	TUD-L [29] \uparrow	YCB-V [70] \uparrow	Mean \uparrow	Time (s) \downarrow
PPF [16]	None	PC	Image	29.7	14.8	38.3	27.6	11.8
FPFH+MAC [54, 75]	None	PC	Image	22.5	22.1	49.6	31.4	136.9
FPFH+RANSAC [19, 54]	None	PC	Image	31.0	31.0	50.0	37.3	6.4
PPF+ICP [2, 16]	None	PC	Image	44.7	29.1	<u>66.8</u>	46.9	14.3
Robust OT [55]	None	PC+RGB	Image	45.5	66.3	66.0	59.3	4.0
FreeZe [4]	None	PC+RGB	Image	45.5	<u>68.3</u>	65.5	59.8	53.0
Dustbin OT [13]	None	PC+RGB	Image	<u>50.2</u>	67.6	65.4	<u>61.1</u>	4.2
COG (Unsupervised)	None	PC+RGB	Image	56.7	73.8	75.9	68.8	4.0
RPM-Net [72]	GT Pose	PC	Image	38.9	28.0	23.8	30.2	3.2
FCGF+MAC [11, 75]	GT Pose	PC	Image	33.9	48.3	51.0	44.4	60.5
FCGF+RANSAC [11, 19]	GT Pose	PC	Image	38.9	59.0	57.6	51.8	11.0
GeDi [50]	GT Pose	PC	Image	42.8	67.3	60.6	56.9	48.9
SAM-6D [39]	GT Pose	PC+RGB	Posed Image	54.5	29.7	68.1	50.8	4.2
UnoPose [41]	GT Pose	PC+RGB	Image	<u>58.7</u>	<u>71.0</u>	83.1	<u>70.9</u>	<u>3.7</u>
COG (Supervised)	GT Pose	PC+RGB	Image	60.8	80.0	<u>80.5</u>	73.8	4.0

Table 1. Quantitative comparison of single-reference novel object pose estimation methods on LM-O, TUD-L, and YCB-V. COG achieves state-of-the-art performance in both supervised and unsupervised settings, with comparable inference speed.

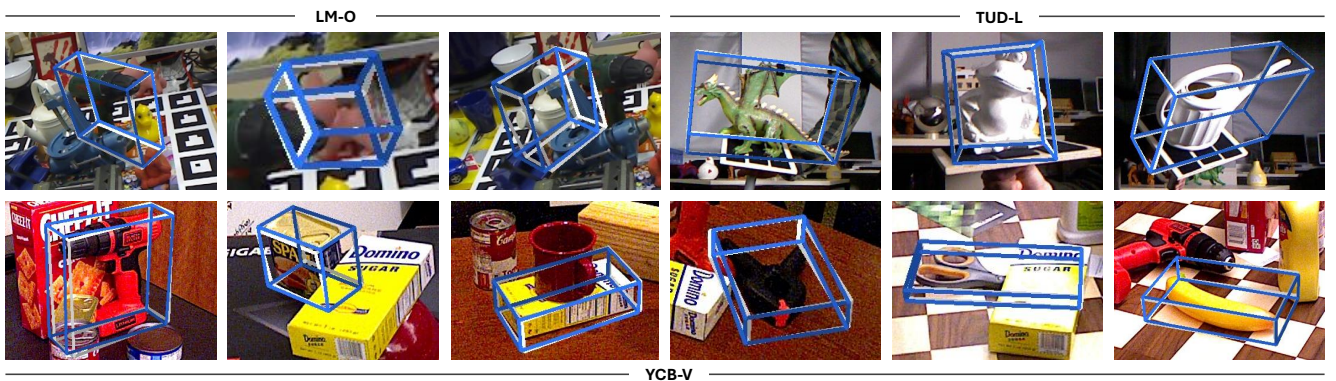


Figure 4. Qualitative results of unsupervised COG on LM-O, TUD-L, and YCB-V datasets. Blue bounding boxes represent the estimated poses, while white boxes denote ground-truth poses.

Method	Dragon	Frog	Watering Can	Mean
UnoPose [41]	70.0	72.2	59.1	67.1
COG (Supervised)	72.9	<u>68.3</u>	83.9	75.0
COG (Unsupervised)	<u>71.2</u>	64.4	<u>81.2</u>	<u>72.3</u>

Table 2. Overlapping IoU results on TUD-L benchmark’s objects.

on the YCB-V benchmark. As shown in Tab. 3, both uniform-marginal OT and our confidence-marginal OT outperform the argmax and softmax baselines by roughly 2–3%, demonstrating the advantage of globally balanced correspondences over discrete or row-normalized mappings. Among OT-based variants, the confidence-marginal formulation further improves the mean performance, validating the effectiveness of incorporating learned confidences as non-uniform marginals. And regarding the loss terms, adding \mathcal{L}_{sem} consistently improves the MSSD and MSPD metrics, while \mathcal{L}_{cycl} mainly benefits VSD, indicating that semantic consistency enhances geometric alignment, and cycle consistency improves visible-region correspondence.

	Correspondence	\mathcal{L}_{sem}	\mathcal{L}_{cycl}	VSD \uparrow	MSSD \uparrow	MSPD \uparrow	Mean \uparrow
A1)	Argmax			71.3	78.4	64.4	71.4
A2)	Argmax		✓	72.1	78.5	64.2	71.6
A3)	Argmax	✓		68.3	79.1	64.0	70.5
A4)	Argmax	✓	✓	73.4	80.0	65.9	73.1
S1)	Softmax			71.9	78.6	64.0	71.5
S2)	Softmax		✓	72.1	78.5	64.1	71.6
S3)	Softmax	✓		68.6	78.3	63.5	70.1
S4)	Softmax	✓	✓	73.4	79.8	65.8	73.0
U1)	Uniform OT			74.6	80.2	67.8	74.2
U2)	Uniform OT		✓	75.0	80.0	67.0	74.0
U3)	Uniform OT	✓		74.1	<u>82.1</u>	69.0	75.0
U4)	Uniform OT	✓	✓	<u>75.8</u>	81.5	68.4	75.2
C1)	Confidence OT			74.8	80.3	67.9	74.3
C2)	Confidence OT		✓	75.5	80.3	67.4	74.4
C3)	Confidence OT	✓		74.9	82.5	69.6	75.6
C4)	Confidence OT	✓	✓	76.5	82.0	<u>69.1</u>	75.9

Table 3. Modules and losses ablation on YCB-V benchmark. Correspondence refers to whether use argmax, softmax, uniform marginal OT, or confidence marginal OT to estimate correspondence, \mathcal{L}_{sem} and \mathcal{L}_{cycl} refer to the use of these loss terms.

Overall, the combination of confidence marginal OT with both auxiliary losses yields the best mean performance.



Figure 5. Visualization of predicted confidence from unsupervised COG. Our method effectively handles non-overlapping regions and outlier points by assigning low confidence to unreliable points. Poses are aligned for visualization.

	Sinkhorn Iteration	Semantic Priors	mAP \uparrow	ENT \downarrow	Δ Marginal \downarrow
C4-1g)	1		73.1	21.1	0.35
C4-2g)	2		73.2	23.0	0.27
C4-4g)	4		73.2	24.1	<u>0.21</u>
C4-8g)	8		73.0	25.7	0.16
C4-1s)	1	✓	<u>75.8</u>	9.2	0.48
C4-2s)	2	✓	75.9	<u>10.5</u>	0.38
C4-4s)	4	✓	<u>75.8</u>	11.4	0.29
C4-8s)	8	✓	75.7	12.0	0.23

Table 4. OT parameters ablation on YCB-V benchmark. Effective Number of Tokens (ENT) reflects the number of points receiving attention, lower values indicate sharper focus. Δ Marginal indicates the distance between target marginals and result marginals.

4.3.2. OT Parameters

We further analyze the influence of parameters in the OT formulation, as summarized in Tab. 4. We use the Effective Number of Tokens (ENT), defined as the exponential of correspondence entropy, to measure the concentration of the transport plan—lower values indicate sharper, more focused correspondences. We also report Δ Marginal, the mean distance between target and resulting marginals, which reflects the marginal alignment quality. When semantic priors are injected into the affinity kernel, mAP improves notably while ENT decreases, indicating that correspondences become more compact and semantically coherent. This confirms that semantic guidance helps the OT solver focus on meaningful, consistent regions across views. In contrast, increasing the number of Sinkhorn iterations beyond two slightly reduces performance. Although additional iterations reduce Δ Marginal, they also make the correspondence map more diffuse, which weakens the geometric precision of the convex combination. Considering this trade-off, we adopt two iterations in our final setting to balance OT marginal accuracy and correspondence sharpness.

4.3.3. Iterative Refinement

We further evaluate the performance gain and computational overhead introduced by iterative refinement on a single NVIDIA RTX 3090 GPU. As shown in Fig. 6, increasing the number of refinement iterations consistently

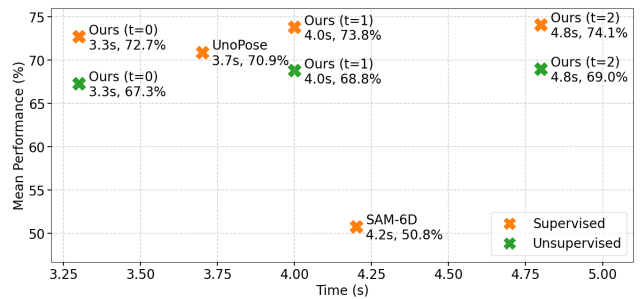


Figure 6. Performance vs runtime (including segmentation, DINO feature extraction, and pose estimation). t indicates the number of refinement iterations.

improves mean performance, though with diminishing returns. A single refinement already boosts both supervised and unsupervised COG by over 1%, while the improvement becomes marginal beyond two iterations. Considering the trade-off between runtime and accuracy, we adopt one refinement iteration as our default setting.

5. Conclusion

We presented Confidence-aware Optimal Geometric Correspondence (COG), an unsupervised framework for single reference novel object pose estimation by solving a confidence-aware optimal transport problem. COG achieves balanced and robust correspondences that improve pose accuracy under occlusions by integrating point-wise confidence as transport marginals. And incorporating semantic priors from vision foundation models further enhances its semantic consistency. Furthermore, the confidence learned in an unsupervised manner from geometric, semantic, and cycle consistency enables COG to down-weight unreliable regions without external labels. Extensive experiments demonstrate that COG achieves performance comparable to state-of-the-art supervised approaches, validating the effectiveness of our unsupervised formulation. Overall, COG provides a principled and scalable direction toward generalizable, unsupervised object pose estimation.

References

- [1] K. S. Arun, T. S. Huang, and S. D. Blostein. Least-squares fitting of two 3-d point sets. *IEEE Transactions on Pattern Analysis and Machine Intelligence*, PAMI-9(5):698–700, 1987. 3
- [2] PJ Besl and Neil D McKay. A method for registration of 3-d shapes. *IEEE Transactions on Pattern Analysis and Machine Intelligence*, 14(2):239–256, 1992. 3, 7
- [3] Eric Brachmann, Alexander Krull, Frank Michel, Stefan Gumhold, Jamie Shotton, and Carsten Rother. Learning 6d object pose estimation using 3d object coordinates. In *Proceedings of European Conference on Computer Vision (ECCV)*, pages 536–551. Springer, 2014. 6, 7, 2, 3, 4
- [4] Andrea Caraffa, Davide Boscaini, Amir Hamza, and Fabio Poiesi. Freeze: Training-free zero-shot 6d pose estimation with geometric and vision foundation models. In *Proceedings of European Conference on Computer Vision (ECCV)*, pages 414–431. Springer, 2024. 2, 7
- [5] Mathilde Caron, Hugo Touvron, Ishan Misra, Hervé Jégou, Julien Mairal, Piotr Bojanowski, and Armand Joulin. Emerging properties in self-supervised vision transformers. In *Proceedings of International Conference on Computer Vision (ICCV)*, pages 9650–9660, 2021. 2
- [6] Angel X Chang, Thomas Funkhouser, Leonidas Guibas, Pat Hanrahan, Qixing Huang, Zimo Li, Silvio Savarese, Manolis Savva, Shuran Song, Hao Su, et al. Shapenet: An information-rich 3d model repository. *arXiv preprint arXiv:1512.03012*, 2015. 6
- [7] Yuchen Che, Ryo Furukawa, and Asako Kanezaki. Op-align: Object-level and part-level alignment for self-supervised category-level articulated object pose estimation. In *Proceedings of European Conference on Computer Vision (ECCV)*, pages 72–88. Springer, 2024. 1, 2
- [8] Haiwei Chen, Shichen Liu, Weikai Chen, Hao Li, and Randall Hill. Equivariant point network for 3d point cloud analysis. In *Proceedings of IEEE Conference on Computer Vision and Pattern Recognition (CVPR)*, pages 14514–14523, 2021. 2
- [9] Kai Chen, Yiyao Ma, Xingyu Lin, Stephen James, Jianshu Zhou, Yun-Hui Liu, Pieter Abbeel, and Qi Dou. Vision foundation model enables generalizable object pose estimation. In *Proceedings of Advances in Neural Information Processing Systems (NeurIPS)*, pages 19975–20002, 2024. 1, 2
- [10] Wei Chen, Xi Jia, Hyung Jin Chang, Jinming Duan, Linlin Shen, and Ales Leonardis. Fs-net: Fast shape-based network for category-level 6d object pose estimation with decoupled rotation mechanism. In *Proceedings of IEEE Conference on Computer Vision and Pattern Recognition (CVPR)*, pages 1581–1590, 2021. 2
- [11] Christopher Choy, Jaesik Park, and Vladlen Koltun. Fully convolutional geometric features. In *Proceedings of International Conference on Computer Vision (ICCV)*, pages 8958–8966, 2019. 3, 7
- [12] Christopher Choy, Wei Dong, and Vladlen Koltun. Deep global registration. In *Proceedings of IEEE Conference on Computer Vision and Pattern Recognition (CVPR)*, 2020. 3
- [13] Zheng Dang, Fei Wang, and Mathieu Salzmann. Learning 3d-3d correspondences for one-shot partial-to-partial registration. *arXiv preprint arXiv:2006.04523*, 2020. 2, 3, 6, 7
- [14] Yan Di, Ruida Zhang, Zhiqiang Lou, Fabian Manhardt, Xiangyang Ji, Nassir Navab, and Federico Tombari. Gpv-pose: Category-level object pose estimation via geometry-guided point-wise voting. In *Proceedings of IEEE Conference on Computer Vision and Pattern Recognition (CVPR)*, pages 6781–6791, 2022. 2
- [15] Laura Downs, Anthony Francis, Nate Koenig, Brandon Kinman, Ryan Hickman, Krista Reymann, Thomas B McHugh, and Vincent Vanhoucke. Google scanned objects: A high-quality dataset of 3d scanned household items. In *Proceedings of IEEE International Conference on Robotics and Automation (ICRA)*, pages 2553–2560. IEEE, 2022. 6
- [16] Bertram Drost, Markus Ulrich, Nassir Navab, and Slobodan Ilic. Model globally, match locally: Efficient and robust 3d object recognition. In *Proceedings of IEEE Conference on Computer Vision and Pattern Recognition (CVPR)*, pages 998–1005. Ieee, 2010. 3, 7
- [17] Y. Eldar, M. Lindenbaum, M. Porat, and Y.Y. Zeevi. The farthest point strategy for progressive image sampling. *IEEE Transactions on Image Processing*, 6(9):1305–1315, 1997. 3, 6
- [18] Zhiwen Fan, Panwang Pan, Peihao Wang, Yifan Jiang, Dejia Xu, and Zhangyang Wang. Pope: 6-dof promptable pose estimation of any object in any scene with one reference. In *Proceedings of IEEE Conference on Computer Vision and Pattern Recognition (CVPR)*, pages 7771–7781, 2024. 1, 2
- [19] Martin A Fischler and Robert C Bolles. Random sample consensus: a paradigm for model fitting with applications to image analysis and automated cartography. *Communications of the ACM*, 24(6):381–395, 1981. 3, 7
- [20] Bowen Fu, Sek Kun Leong, Xiaocong Lian, and Xiangyang Ji. 6d robotic assembly based on rgb-only object pose estimation. In *Proceedings of IEEE/RSJ International Conference on Intelligent Robots and Systems (IROS)*, pages 4736–4742. IEEE, 2022. 1
- [21] Bowen Fu, Sek Kun Leong, Yan Di, Gu Wang, Jiwen Tang, Federico Tombari, and Xiangyang Ji. Lanpose: Language-instructed 6d object pose estimation for robotic assembly. In *Proceedings of European Conference on Computer Vision (ECCV)*, pages 43–59. Springer, 2024. 1
- [22] Yang Fu and Xiaolong Wang. Category-level 6d object pose estimation in the wild: A semi-supervised learning approach and a new dataset. *Proceedings of Advances in Neural Information Processing Systems (NeurIPS)*, 35:27469–27483, 2022. 2
- [23] Wei Gao and Russ Tedrake. Filterreg: Robust and efficient probabilistic point-set registration using gaussian filter and twist parameterization. In *Proceedings of IEEE Conference on Computer Vision and Pattern Recognition (CVPR)*, pages 11095–11104, 2019. 3
- [24] Walter Goodwin, Sagar Vaze, Ioannis Havoutis, and Ingmar Posner. Zero-shot category-level object pose estimation. In *Proceedings of European Conference on Computer Vision (ECCV)*, pages 516–532. Springer, 2022. 2

- [25] Mark Hamilton, Zhoutong Zhang, Bharath Hariharan, Noah Snavely, and William T. Freeman. Unsupervised semantic segmentation by distilling feature correspondences. In *Proceedings of International Conference on Learning Representations (ICLR)*, 2022. 5, 1
- [26] Rasmus Laurvig Haugaard and Anders Glent Buch. Surfemb: Dense and continuous correspondence distributions for object pose estimation with learnt surface embeddings. In *Proceedings of IEEE Conference on Computer Vision and Pattern Recognition (CVPR)*, pages 6749–6758, 2022. 2
- [27] Xingyi He, Jiaming Sun, Yuang Wang, Di Huang, Hujun Bao, and Xiaowei Zhou. Onepose++: Keypoint-free one-shot object pose estimation without cad models. *Proceedings of Advances in Neural Information Processing Systems (NeurIPS)*, 35:35103–35115, 2022. 1, 2
- [28] Yisheng He, Haibin Huang, Haoqiang Fan, Qifeng Chen, and Jian Sun. Ffb6d: A full flow bidirectional fusion network for 6d pose estimation. In *Proceedings of IEEE Conference on Computer Vision and Pattern Recognition (CVPR)*, pages 3003–3013, 2021. 1, 2
- [29] Tomas Hodan, Frank Michel, Eric Brachmann, Wadim Kehl, Anders GlentBuch, Dirk Kraft, Bertram Drost, Joel Vidal, Stephan Ihrke, Xenophon Zabulis, et al. Bop: Benchmark for 6d object pose estimation. In *Proceedings of European Conference on Computer Vision (ECCV)*, pages 19–34, 2018. 6, 7, 2, 3, 4
- [30] Siyuan Huang, Siyuan Qi, Yinxue Xiao, Yixin Zhu, Ying Nian Wu, and Song-Chun Zhu. Cooperative holistic scene understanding: Unifying 3d object, layout, and camera pose estimation. *Proceedings of Advances in Neural Information Processing Systems (NeurIPS)*, 31, 2018. 1
- [31] Muhammad Zubair Irshad, Thomas Kollar, Michael Laskey, Kevin Stone, and Zsolt Kira. Centersnap: Single-shot multi-object 3d shape reconstruction and categorical 6d pose and size estimation. In *Proceedings of IEEE International Conference on Robotics and Automation (ICRA)*, pages 10632–10640. IEEE, 2022. 2
- [32] Muhammad Zubair Irshad, Sergey Zakharov, Rares Ambrus, Thomas Kollar, Zsolt Kira, and Adrien Gaidon. Shapo: Implicit representations for multi-object shape, appearance, and pose optimization. In *Proceedings of European Conference on Computer Vision (ECCV)*, pages 275–292. Springer, 2022. 1, 2
- [33] Diederik P Kingma. Adam: A method for stochastic optimization. *arXiv preprint arXiv:1412.6980*, 2014. 6
- [34] Alexander Kirillov, Eric Mintun, Nikhila Ravi, Hanzi Mao, Chloe Rolland, Laura Gustafson, Tete Xiao, Spencer Whitehead, Alexander C Berg, Wan-Yen Lo, et al. Segment anything. In *Proceedings of International Conference on Computer Vision (ICCV)*, pages 4015–4026, 2023. 2
- [35] Yann Labbé, Lucas Manuelli, Arsalan Mousavian, Stephen Tyree, Stan Birchfield, Jonathan Tremblay, Justin Carpentier, Mathieu Aubry, Dieter Fox, and Josef Sivic. Megapose: 6d pose estimation of novel objects via render & compare. *arXiv preprint arXiv:2212.06870*, 2022. 1, 2, 6
- [36] Vincent Lepetit, Francesc Moreno-Noguer, and Pascal Fua. Ep n p: An accurate o (n) solution to the p n p problem. *International Journal of Computer Vision*, 81(2):155–166, 2009. 2
- [37] Jiahao Li, Changhao Zhang, Ziyao Xu, Hangning Zhou, and Chi Zhang. Iterative distance-aware similarity matrix convolution with mutual-supervised point elimination for efficient point cloud registration. In *Proceedings of European Conference on Computer Vision (ECCV)*, pages 378–394. Springer, 2020. 3
- [38] Xiaolong Li, Yijia Weng, Li Yi, Leonidas J Guibas, A Abbott, Shuran Song, and He Wang. Leveraging se (3) equivariance for self-supervised category-level object pose estimation from point clouds. *Proceedings of Advances in Neural Information Processing Systems (NeurIPS)*, 34:15370–15381, 2021. 2
- [39] Jiehong Lin, Lihua Liu, Dekun Lu, and Kui Jia. Sam-6d: Segment anything model meets zero-shot 6d object pose estimation. In *Proceedings of IEEE Conference on Computer Vision and Pattern Recognition (CVPR)*, pages 27906–27916, 2024. 1, 2, 6, 7, 3
- [40] Jian Liu, Wei Sun, Kai Zeng, Jin Zheng, Hui Yang, Hossein Rahmani, Ajmal Mian, and Lin Wang. Novel object 6d pose estimation with a single reference view. *arXiv preprint arXiv:2503.05578*, 2025. 1, 2
- [41] Xingyu Liu, Gu Wang, Ruida Zhang, Chenyangguang Zhang, Federico Tombari, and Xiangyang Ji. Unopose: Unseen object pose estimation with an unposed rgb-d reference image. In *Proceedings of IEEE Conference on Computer Vision and Pattern Recognition (CVPR)*, pages 22023–22034, 2025. 1, 2, 3, 6, 7
- [42] Eric Marchand, Hideaki Uchiyama, and Fabien Spindler. Pose estimation for augmented reality: a hands-on survey. *IEEE Transactions on Visualization and Computer Graphics*, 22(12):2633–2651, 2015. 1
- [43] Guofeng Mei, Hao Tang, Xiaoshui Huang, Weijie Wang, Juan Liu, Jian Zhang, Luc Van Gool, and Qiang Wu. Unsupervised deep probabilistic approach for partial point cloud registration. In *Proceedings of IEEE Conference on Computer Vision and Pattern Recognition (CVPR)*, pages 13611–13620, 2023. 3
- [44] Sunghill Moon, Hyeontae Son, Dongcheol Hur, and Sangwook Kim. Genflow: Generalizable recurrent flow for 6d pose refinement of novel objects. In *Proceedings of IEEE Conference on Computer Vision and Pattern Recognition (CVPR)*, pages 10039–10049, 2024. 1, 2
- [45] Van Nguyen Nguyen, Thibault Groueix, Georgy Ponimatkin, Vincent Lepetit, and Tomas Hodan. Cnos: A strong baseline for cad-based novel object segmentation. In *Proceedings of International Conference on Computer Vision (ICCV)*, pages 2134–2140, 2023. 2, 3
- [46] Van Nguyen Nguyen, Thibault Groueix, Georgy Ponimatkin, Yinlin Hu, Renaud Marlet, Mathieu Salzmann, and Vincent Lepetit. Nope: Novel object pose estimation from a single image. In *Proceedings of IEEE Conference on Computer Vision and Pattern Recognition (CVPR)*, pages 17923–17932, 2024. 1, 2
- [47] Van Nguyen Nguyen, Thibault Groueix, Mathieu Salzmann, and Vincent Lepetit. Gigapose: Fast and robust novel object

- pose estimation via one correspondence. In *Proceedings of IEEE Conference on Computer Vision and Pattern Recognition (CVPR)*, pages 9903–9913, 2024. 2
- [48] Maxime Oquab, Timothée Darcet, Théo Moutakanni, Huy Vo, Marc Szafraniec, Vasil Khalidov, Pierre Fernandez, Daniel Haziza, Francisco Massa, Alaaeldin El-Nouby, et al. Dinov2: Learning robust visual features without supervision. *arXiv preprint arXiv:2304.07193*, 2023. 2, 3, 5, 1
- [49] G Dias Pais, Srikumar Ramalingam, Venu Madhav Govindu, Jacinto C Nascimento, Rama Chellappa, and Pedro Miraldo. 3dregnet: A deep neural network for 3d point registration. In *Proceedings of IEEE Conference on Computer Vision and Pattern Recognition (CVPR)*, pages 7193–7203, 2020. 3
- [50] Fabio Poiesi and Davide Boscaini. Learning general and distinctive 3d local deep descriptors for point cloud registration. *IEEE Transactions on Pattern Analysis and Machine Intelligence*, 45(3):3979–3985, 2022. 7
- [51] Zheng Qin, Hao Yu, Changjian Wang, Yulan Guo, Yuxing Peng, and Kai Xu. Geometric transformer for fast and robust point cloud registration. In *Proceedings of IEEE Conference on Computer Vision and Pattern Recognition (CVPR)*, pages 11143–11152, 2022. 3, 6
- [52] Alec Radford, Jong Wook Kim, Chris Hallacy, Aditya Ramesh, Gabriel Goh, Sandhini Agarwal, Girish Sastry, Amanda Askell, Pamela Mishkin, Jack Clark, et al. Learning transferable visual models from natural language supervision. In *Proceedings of International Conference on Machine Learning (ICML)*, pages 8748–8763. PmLR, 2021. 2
- [53] Nikhila Ravi, Jeremy Reizenstein, David Novotny, Taylor Gordon, Wan-Yen Lo, Justin Johnson, and Georgia Gkioxari. Accelerating 3d deep learning with pytorch3d. *arXiv:2007.08501*, 2020. 5
- [54] Radu Bogdan Rusu, Nico Blodow, and Michael Beetz. Fast point feature histograms (fpfh) for 3d registration. In *Proceedings of IEEE International Conference on Robotics and Automation (ICRA)*, pages 3212–3217. IEEE, 2009. 3, 7
- [55] Zhengyang Shen, Jean Feydy, Peirong Liu, Ariel H Curiale, Ruben San Jose Estepar, Raul San Jose Estepar, and Marc Niethammer. Accurate point cloud registration with robust optimal transport. *Proceedings of Advances in Neural Information Processing Systems (NeurIPS)*, 34:5373–5389, 2021. 2, 3, 6, 7
- [56] Richard Sinkhorn. A relationship between arbitrary positive matrices and doubly stochastic matrices. *The annals of mathematical statistics*, 35(2):876–879, 1964. 3, 4, 1
- [57] Yongzhi Su, Jason Rambach, Nareg Minaskan, Paul Lesur, Alain Pagani, and Didier Stricker. Deep multi-state object pose estimation for augmented reality assembly. In *IEEE International Symposium on Mixed and Augmented Reality Adjunct (ISMAR-Adjunct)*, pages 222–227. IEEE, 2019. 1
- [58] Jiaming Sun, Zihao Wang, Siyu Zhang, Xingyi He, Hongcheng Zhao, Guofeng Zhang, and Xiaowei Zhou. Onepose: One-shot object pose estimation without cad models. In *Proceedings of IEEE Conference on Computer Vision and Pattern Recognition (CVPR)*, pages 6825–6834, 2022. 1, 2
- [59] Martin Sundermeyer, Zoltan-Csaba Marton, Maximilian Durner, and Rudolph Triebel. Augmented autoencoders: Implicit 3d orientation learning for 6d object detection. *International Journal of Computer Vision*, 128:714–729, 2020. 2
- [60] Martin Sundermeyer, Tomáš Hodaň, Yann Labbe, Gu Wang, Eric Brachmann, Bertram Drost, Carsten Rother, and Jiří Matas. Bop challenge 2022 on detection, segmentation and pose estimation of specific rigid objects. In *Proceedings of IEEE Conference on Computer Vision and Pattern Recognition (CVPR)*, pages 2785–2794, 2023. 6
- [61] Meng Tian, Marcelo H Ang, and Gim Hee Lee. Shape prior deformation for categorical 6d object pose and size estimation. In *Proceedings of European Conference on Computer Vision (ECCV)*, 2020. 2
- [62] Jonathan Tremblay, Thang To, Balakumar Sundaralingam, Yu Xiang, Dieter Fox, and Stan Birchfield. Deep object pose estimation for semantic robotic grasping of household objects. *arXiv preprint arXiv:1809.10790*, 2018. 1
- [63] Shinji Umeyama. Least-squares estimation of transformation parameters between two point patterns. *IEEE Transactions on Pattern Analysis and Machine Intelligence*, 13(04):376–380, 1991. 2, 3, 5
- [64] Chen Wang, Danfei Xu, Yuke Zhu, Roberto Martín-Martín, Cewu Lu, Li Fei-Fei, and Silvio Savarese. Densefusion: 6d object pose estimation by iterative dense fusion. In *Proceedings of IEEE Conference on Computer Vision and Pattern Recognition (CVPR)*, pages 3343–3352, 2019. 1, 2
- [65] Gu Wang, Fabian Manhardt, Jianzhun Shao, Xiangyang Ji, Nassir Navab, and Federico Tombari. Self6d: Self-supervised monocular 6d object pose estimation. In *Proceedings of European Conference on Computer Vision (ECCV)*, pages 108–125. Springer, 2020. 2
- [66] Gu Wang, Fabian Manhardt, Federico Tombari, and Xiangyang Ji. Gdr-net: Geometry-guided direct regression network for monocular 6d object pose estimation. In *Proceedings of IEEE Conference on Computer Vision and Pattern Recognition (CVPR)*, pages 16611–16621, 2021. 1, 2
- [67] He Wang, Srinath Sridhar, Jingwei Huang, Julien Valentin, Shuran Song, and Leonidas J Guibas. Normalized object coordinate space for category-level 6d object pose and size estimation. In *Proceedings of IEEE Conference on Computer Vision and Pattern Recognition (CVPR)*, pages 2642–2651, 2019. 1, 2
- [68] Pengyuan Wang, Takuya Ikeda, Robert Lee, and Koichi Nishiwaki. Gs-pose: Category-level object pose estimation via geometric and semantic correspondence. In *Proceedings of European Conference on Computer Vision (ECCV)*, pages 108–126. Springer, 2024. 1, 2
- [69] Tong Wu, Liang Pan, Junzhe Zhang, Tai Wang, Ziwei Liu, and Dahua Lin. Density-aware chamfer distance as a comprehensive metric for point cloud completion, 2021. 5
- [70] Yu Xiang, Tanner Schmidt, Venkatraman Narayanan, and Dieter Fox. Posecnn: A convolutional neural network for 6d object pose estimation in cluttered scenes. *arXiv preprint arXiv:1711.00199*, 2017. 6, 7, 2, 3, 4
- [71] Li Xu, Haoxuan Qu, Yujun Cai, and Jun Liu. 6d-diff: A keypoint diffusion framework for 6d object pose estimation. In *Proceedings of IEEE Conference on Computer Vision and Pattern Recognition (CVPR)*, pages 9676–9686, 2024. 1, 2

- [72] Zi Jian Yew and Gim Hee Lee. Rpm-net: Robust point matching using learned features. In *Proceedings of IEEE Conference on Computer Vision and Pattern Recognition (CVPR)*, pages 11824–11833, 2020. [2](#), [3](#), [6](#), [7](#)
- [73] Yongzhe Yuan, Yue Wu, Xiaolong Fan, Maoguo Gong, Qiguang Miao, and Wenping Ma. Inlier confidence calibration for point cloud registration. In *Proceedings of IEEE Conference on Computer Vision and Pattern Recognition (CVPR)*, pages 5312–5321, 2024. [3](#)
- [74] Jiayao Zhang, Weiyao Huang, Bo Peng, Mingdong Wu, Fei Hu, Zijian Chen, Bo Zhao, and Hao Dong. Omni6dpose: A benchmark and model for universal 6d object pose estimation and tracking. In *Proceedings of European Conference on Computer Vision (ECCV)*, pages 199–216. Springer, 2024. [1](#)
- [75] Xiyu Zhang, Jiaqi Yang, Shikun Zhang, and Yanning Zhang. 3d registration with maximal cliques. In *Proceedings of IEEE Conference on Computer Vision and Pattern Recognition (CVPR)*, pages 17745–17754, 2023. [7](#)
- [76] Xu Zhao, Wenchao Ding, Yongqi An, Yinglong Du, Tao Yu, Min Li, Ming Tang, and Jinqiao Wang. Fast segment anything. *arXiv preprint arXiv:2306.12156*, 2023. [2](#)
- [77] Linfang Zheng, Chen Wang, Yinghan Sun, Esha Dasgupta, Hua Chen, Aleš Leonardis, Wei Zhang, and Hyung Jin Chang. Hs-pose: Hybrid scope feature extraction for category-level object pose estimation. In *Proceedings of IEEE Conference on Computer Vision and Pattern Recognition (CVPR)*, pages 17163–17173, 2023. [2](#)
- [78] Jun-Yan Zhu, Taesung Park, Phillip Isola, and Alexei A Efros. Unpaired image-to-image translation using cycle-consistent adversarial networks. In *Proceedings of International Conference on Computer Vision (ICCV)*, pages 2223–2232, 2017. [4](#)
- [79] Minghan Zhu, Maani Ghaffari, William A Clark, and Huei Peng. E2pn: Efficient se (3)-equivariant point network. In *Proceedings of IEEE Conference on Computer Vision and Pattern Recognition (CVPR)*, pages 1223–1232, 2023. [2](#)

COG: Confidence-aware Optimal Geometric Correspondence for Unsupervised Single-reference Novel Object Pose Estimation

Supplementary Material

Contents

- **Section A: Model Details**
 - A.1: Sinkhorn and Affinity Kernel
 - A.2: Semantic Denoising
 - A.3: Pseudo Confidence Labels
- **Section B: Experiment Details**
 - B.1: Data Efficiency Analysis
 - B.2: Confidence Analysis
 - B.3: Symmetry Analysis
 - B.4: Extended Results and Visualizations
- **Section C: Limitations**
 - C.1: Segmentation Failure
 - C.2: Unsupervised Limitation

A. Model Details

A.1. Sinkhorn and Affinity Kernel

To compute differentiable cross-view correspondences under non-uniform confidence marginals, we adopt the entropy-regularized optimal transport (OT) framework with a log-domain Sinkhorn [56] solver. Let $\mathbf{K} \in \mathbb{R}^{n \times n}$ denote the affinity matrix, and let $\mathbf{w}_{\text{row}} = \mathbf{w}_p, \mathbf{w}_{\text{col}} = \mathbf{w}_q$ be the target marginals obtained by normalizing point-wise confidences from the query and reference point clouds. The Sinkhorn algorithm iteratively updates the dual variables $\mathbf{u}, \mathbf{v} \in \mathbb{R}^n$ and recovers a transport plan satisfying the prescribed marginals (Alg. 1). The log-sum-exp implementation ensures numerical stability and prevents underflow in high-dimensional spaces.

For explanatory decomposition, we first define the OT cost as the negative similarity, and decompose the OT cost into a geometric similarity term and a nonlinear scaled semantic consistency term:

$$\mathbf{C}_{[i,j]} = -\langle \mathbf{G}_{p[i]}, \mathbf{G}_{q[j]} \rangle_{\text{cos}} - \lambda \log(1 + \langle \mathbf{S}_{p[i]}, \mathbf{S}_{q[j]} \rangle_{\text{cos}}), \quad (11)$$

where the semantic term is expressed in a logarithmic form. This design yields a semantic modulation that encourages semantically coherent matches without overwhelming the geometric similarity when semantic features are relatively similar. On the other hand, when the semantic similarity becomes negative, it yields a strong penalty for semantically inconsistent matches. This nonlinear shape prevents excessive amplification for already similar semantic pairs, while still sharply suppressing mismatched or unrelated regions. In practice, since cosine similarity may take negative values close to -1 and $\log(1+x)$ close to $-\infty$, a small stability

Algorithm 1 Log-Domain Sinkhorn with Target Marginals

- 1: **Input:** affinity \mathbf{K} , marginals $\mathbf{w}_{\text{row}}, \mathbf{w}_{\text{col}}$, iterations T
- 2: **Output:** transport matrix $\mathbf{\Pi}$
- 3: Initialize dual variables: $\mathbf{u} \leftarrow \mathbf{0}^n, \mathbf{v} \leftarrow \mathbf{0}^n$
- 4: **for** $t = 1, \dots, T$ **do**
- 5: $\mathbf{u}_{[i]} \leftarrow \log \mathbf{w}_{\text{row}[i]} - \log \sum_j \exp(\log \mathbf{K}_{[i,j]} + \mathbf{v}_{[j]})$
- 6: $\mathbf{v}_{[j]} \leftarrow \log \mathbf{w}_{\text{col}[j]} - \log \sum_i \exp(\log \mathbf{K}_{[i,j]} + \mathbf{u}_{[i]})$
- 7: **end for**
- 8: Recover transport plan:

$$\mathbf{\Pi}_{[i,j]} = \exp(\log \mathbf{K}_{[i,j]} + \mathbf{u}_{[i]} + \mathbf{v}_{[j]}).$$

constant $\epsilon = 10^{-6}$ is added inside the logarithmic semantic term for stable training. And the regularized OT problem is written as:

$$\min_{\mathbf{\Pi} \geq 0} \langle \mathbf{C}, \mathbf{\Pi} \rangle + \tau \sum_{i,j} \mathbf{\Pi}_{[i,j]} \log \mathbf{\Pi}_{[i,j]}, \quad (12)$$

subject to the constraints $\mathbf{\Pi} \mathbf{1} = \mathbf{w}_{\text{row}}$ and $\mathbf{\Pi}^\top \mathbf{1} = \mathbf{w}_{\text{col}}$. Under entropy regularization, the minimizer admits the Gibbs form $\mathbf{\Pi}_{[i,j]} \propto \exp(-\frac{1}{\tau} \mathbf{C}_{[i,j]})$. Substituting Eq. (11) yields the following factorized affinity kernel:

$$\begin{aligned} \mathbf{K}_{[i,j]} &= \exp(-\frac{1}{\tau} \mathbf{C}_{[i,j]}) \\ &= \exp(\frac{1}{\tau} \langle \mathbf{G}_{p[i]}, \mathbf{G}_{q[j]} \rangle_{\text{cos}}) (1 + \langle \mathbf{S}_{p[i]}, \mathbf{S}_{q[j]} \rangle_{\text{cos}})^{\lambda/\tau}. \end{aligned} \quad (13)$$

which injects geometric affinity with semantic coherence, providing a soft semantic prior.

A.2. Semantic Denoising

As we indicated in main script, we follow STEGO [25] for semantic denoising. Fig. 7 shows the t-SNE embeddings of the raw DINO [48] features F_p, F_q and the denoised semantic features S_p, S_q from the query and reference views. After semantic denoising, features belonging to the same semantic parts from different viewpoints become significantly closer in the embedding space, indicating improved cross-view semantic consistency. This demonstrates that the lightweight semantic head effectively filters view-dependent noise in DINO features and provides more stable guidance for the subsequent OT correspondence.

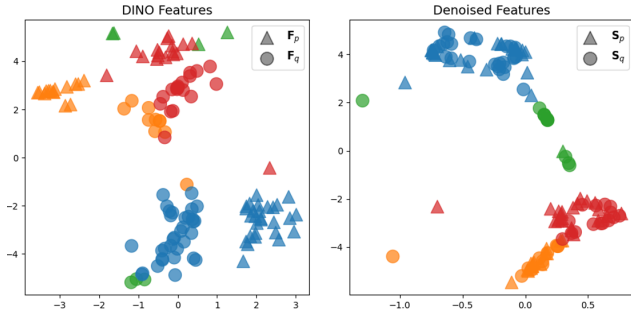


Figure 7. t-SNE results of DINO features on query and reference F_p, F_q , and denoised semantic features S_p, S_q , colored by k-means part segmentation. With semantic denoising, the distance between points from different views (triangle and circle) with the same semantic part is reducing dramatically.

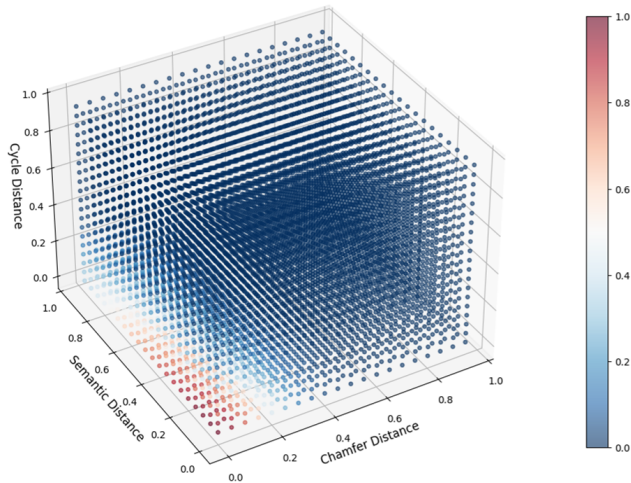


Figure 8. Visualization of pseudo confidence label generation. Points with smaller Chamfer, cycle, and semantic distances receive higher confidence labels.

A.3. Pseudo Confidence Labels

As an essential supervision signal of point validity, pseudo confidence labels are generated from Gaussian kernels defined over geometric ($\phi_{\text{cycl}}, \phi_{\text{pose}}$) and semantic (ϕ_{sem}) distances. As illustrated in Fig. 8, points exhibiting small Chamfer, semantic, and cycle distances are assigned high confidence labels, while inconsistent or noisy points which contains larger distance receive low confidence labels.

With such design, the training process can be interpreted as an EM-like process that unfolds across epochs rather than within a single optimization step. Specifically, the previous training iterations act as the *E-step*, where the network estimates latent variables—soft correspondences and poses—and derives pseudo confidence labels based on the current model state. The current iteration then plays the role of the *M-step*, in which these pseudo confidence labels supervise the confidence branch, guiding the model toward more

Method	LM-O [3]	TUD-L [29]	YCB-V [70]	Mean \uparrow
DINO+PHS [48]	24.7	16.2	45.2	28.7
COG (1% data)	52.9	66.9	73.6	64.5
COG (5% data)	55.7	70.5	75.7	67.3
COG (25% data)	55.1	70.7	75.4	67.2
COG (50% data)	55.4	71.8	74.7	67.3
COG (100% data)	56.7	73.8	75.9	68.8

Table 5. Quantitative comparison of DINO with pose-hypothesis-scoring (PHS) and COG trained with different fractions of the training data.

accurate correspondence and pose estimation within high confidence points. Through this implicit alternating process across iterations, COG progressively reinforces the consistency between confidence, correspondence, and pose, leading to stable performance without external supervision.

Stability. Locality consistency: Intuitively, once a point receives a high pseudo confidence label, its neighboring points, being geometrically close and semantically consistent, naturally inherit similar high confidence labels. This locality-aware consistency propagates stable supervision across nearby regions, making subsequent confidence predictions more coherent over iterations. **Normalized confidence:** To further ensure robustness in early training (when confidence labels are close to zero), all losses except $\mathcal{L}_{\text{conf}}$ are weighted by the normalized confidence $w = c/\bar{c}$ rather than the raw confidence c . Consequently, even if all predicted confidences start near zero, the optimization reduces to a uniform weighting scheme, preventing degenerate gradients and maintaining stable learning dynamics. **Detached labels:** In addition, the pseudo confidence labels used in $\mathcal{L}_{\text{conf}}$ are detached from backpropagation, avoiding harmful feedback loops that would push low confidence points farther.

In practice, with such design, the training process consistently behavior across all datasets, and we observe no signs of collapse or instability.

B. Experiment Details

B.1. Data Efficiency Analysis

As a task requires dataset-agnostic generalization, the data efficiency is important. To evaluate the data efficiency of our model, we train COG with progressively smaller subsets of the training data. Specifically, we randomly sample (1%, 5%, 25%, 50%) of the full training set (2M images) and train our unsupervised model on each subset. For comparison with training-free pure semantic features, we replace the OT module with one-to-one correspondence based on DINO [48] feature similarity and apply a pose-hypothesis-scoring (PHS) scheme, which generates 6,000 pose candidates and selects the one with the highest match-

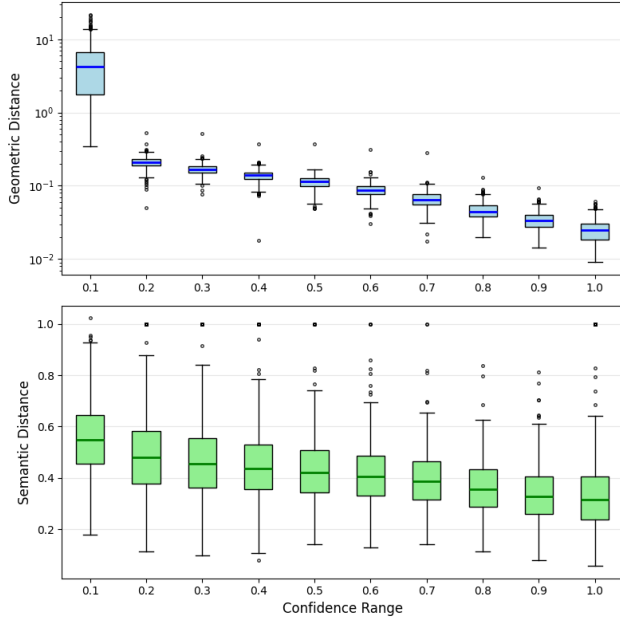


Figure 9. Relationship between predicted confidence and point-level distances for all test query-reference pairs in TUD-L [29] benchmark. The geometric distance (log scale) and semantic cosine distance are measured between each point and its nearest neighbor.

ing score, following the coarse pose selection strategy used in [39, 41].

The results in Tab. 5 show that even with only 1% of the data (about 20k images), our method achieves a substantial performance gain over the DINO baseline, highlighting the importance of geometric reasoning and confidence learning for accurate pose estimation. Interestingly, increasing the data volume beyond 5% leads to only marginal improvements on LM-O [3] and YCB-V [70] benchmarks, while performance on TUD-L [29] benchmark exhibits a more noticeable gain. This difference reflects the characteristics of each benchmark: TUD-L contains objects with complex shapes that benefit from high-precision geometric alignment, whereas LM-O and YCB-V include more texture-rich objects, where semantic priors already provide strong guidance.

Overall, these findings demonstrate that unlike prior approaches relying on large-scale data, CAD models, or pose supervision, COG generalizes effectively even under extremely limited data and unsupervised setting, highlighting the data efficiency of our unsupervised framework.

B.2. Confidence Analysis

To further examine what the predicted confidence captures, we use all query-reference pairs in TUD-L [29], and measure for each point its nearest corresponding point in the

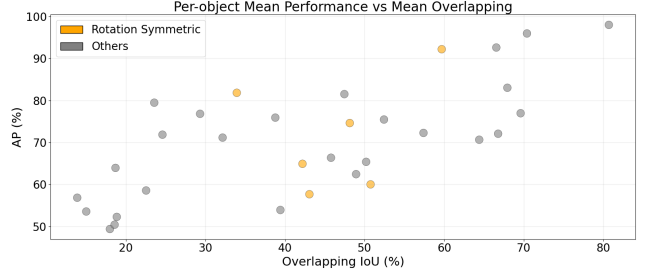


Figure 10. Per-object mean performance and overlapping.

other view and compute two distances: geometric Euclidean distance in 3D space and semantic cosine distance ($1 - \langle \cdot, \cdot \rangle_{\text{cos}}$) in feature space.

As shown in Fig. 9, both geometric and semantic distances show a consistent downward trend as confidence increases, confirming that the confidence branch effectively learns to identify reliable correspondences, by jointly informed from geometric and semantic consistency.

B.3. Symmetry Analysis

For rotationally symmetric objects, such as bottles and bowls, the geometric and semantic features of different points often become indistinguishable. This ambiguity can lead to multiple valid transport solutions and, consequently, inaccurate pose estimation.

To mitigate this risk, we incorporate positional embeddings into the fine-phase geometry encoder to sharpen diffused features. These coordinate-based embeddings provide a soft constraint, biasing the model toward selecting correspondences within a local neighborhood rather than distant, yet geometrically similar, points. Furthermore, points with diffused correspondences typically fail the cycle consistency constraint, resulting in lower confidence scores.

As shown in Fig. 10, our evaluation of objects with identical overlapping ratios demonstrates no significant performance degradation attributable to symmetry.

B.4. Extended Results and Visualizations

In this section, we provide additional quantitative and qualitative results that complement the main experiments presented in the paper. Specifically, we report complete per-object results for all test objects on the LM-O, TUD-L, and YCB-V [3, 29, 70] benchmarks, as shown in Tab. 6. We also include extended visualizations of estimated poses in Fig. 12, illustrating the robustness of COG under varying occlusion levels, viewpoint changes, and object shapes. These extended results further validate the conclusions drawn in the main paper, demonstrating that COG achieves stable and accurate performance across diverse scenarios.

Benchmark	Object	VSD \uparrow	MSSD \uparrow	MSPD \uparrow	Mean \uparrow
LM-O [3]	ape	40.0	54.7	65.5	53.4
	can	51.1	70.2	68.0	63.1
	cat	37.6	53.1	58.1	49.6
	driller	47.7	56.1	51.6	51.8
	duck	53.1	59.2	68.6	60.3
	eggbox	42.9	59.8	63.6	55.4
	glue	38.7	55.2	54.8	49.6
	holepuncher	59.5	69.5	71.7	66.9
	Average	46.9	60.1	63.0	56.7
TUD-L [29]	dragon	64.2	83.3	81.0	76.2
	frog	72.5	74.8	79.4	75.6
	can	58.9	78.3	72.3	69.8
	Average	65.2	78.8	77.6	73.8
YCB-V [70]	master_chef_can	83.0	70.2	42.9	65.4
	cracker_box	71.0	79.6	62.5	71.0
	sugar_box	92.6	97.6	90.5	93.6
	tomato_soup_can	84.9	75.5	64.8	75.0
	mustard_bottle	81.7	89.5	74.6	81.9
	tuna_fish_can	72.8	56.1	53.8	60.9
	pudding_box	92.3	97.6	94.7	94.9
	gelatin_box	97.3	100.0	98.7	98.7
	potted_meat_can	57.4	62.7	55.9	58.7
	banana	75.7	87.7	64.7	76.0
	pitcher_base	87.4	86.5	59.9	77.9
	bleach_cleanser	80.1	88.2	68.0	78.8
	bowl	87.1	97.3	91.1	91.8
	mug	65.5	71.6	67.3	68.1
	power_drill	69.3	87.0	71.3	75.9
	wood_block	86.5	93.7	81.2	87.1
	scissors	51.0	86.4	71.2	69.5
	large_marker	62.6	93.3	89.8	81.9
	large_clamp	62.0	87.5	79.7	76.4
	extra_large_clamp	46.2	78.9	57.9	61.0
foam_brick	80.8	86.4	83.3	83.5	
Average	76.5	82.0	69.1	75.9	

Table 6. Per-object results on the LM-O [3], TUD-L [29], and YCB-V [70] benchmarks.

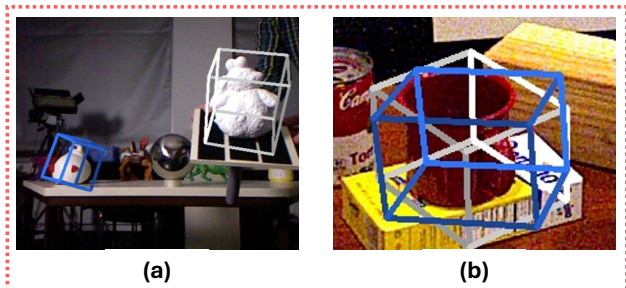


Figure 11. Failure cases of our method. (a) indicates the segmentation failure where segmentation mask is incorrect, and (b) indicates the unsupervised limitation discussed in Sec. C.2.

C. Limitations

C.1. Segmentation Failure

Our framework relies on segmentation model to extract the masked depth for the point cloud inputs in the pre-processing. Therefore, segmentation errors can directly propagate to downstream pose estimation. As shown in Fig. 11 (a), if the segmentation model mistakenly includes

different objects rather than the query object, the resulting point cloud may contain irrelevant geometry that cannot be recovered during pose estimation phase, leading to false correspondences and inaccurate. In future work, integrating joint segmentation-pose optimization may mitigate such cascading errors.

C.2. Unsupervised Limitation

As an unsupervised framework, COG optimizes pose implicitly, mainly through confidence-weighted Chamfer distance. This objective encourages minimizing high confidence point distances rather than explicitly enforcing a globally correct pose transformation. Consequently, when parts of the object contain sparse or noisy points, the network may prioritize aligning dense regions at the expense of small but semantically important parts. For example, as shown in Fig. 11 (b), when estimating the pose of a mug, the handle often contributes only few points; the network may achieve lower overall loss by ignoring this region and aligning only the main body of the mug. Although the introduction of semantic priors alleviates this issue to some extent, such priors remain soft constraints and cannot fully prevent these trade-offs. Future work could explore hybrid supervision or structural regularization (*e.g.* semantic part hard constraints) to better preserve critical fine-grained geometry during unsupervised optimization.

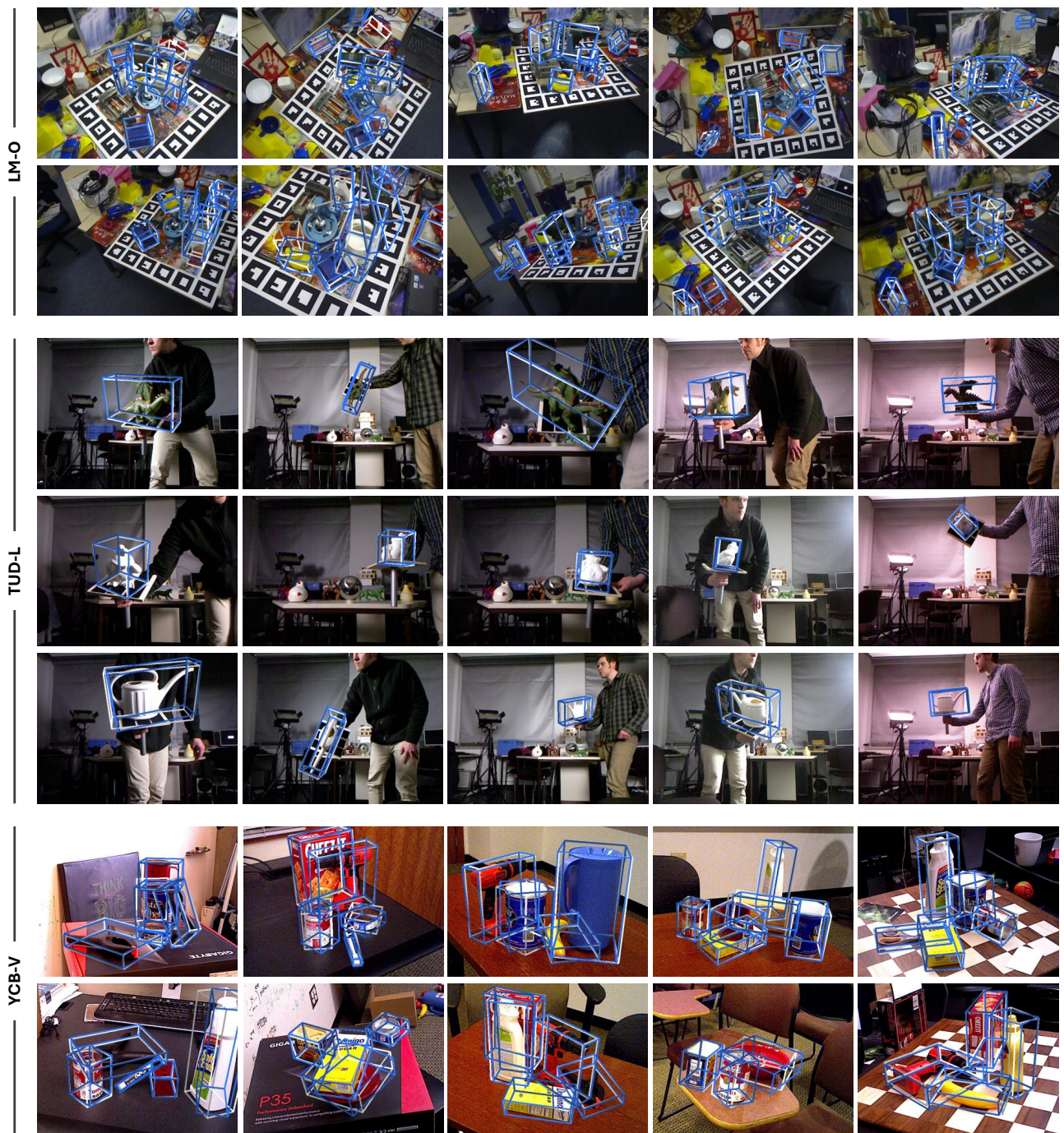


Figure 12. Results on 3 BOP benchmarks. Blue bounding boxes represent the estimated poses, while white boxes denote ground-truth poses.